Hydrogen escaping from a pair of exoplanets smaller than Neptune

https://doi.org/10.1038/s41586-024-08490-x

Received: 16 January 2024

Accepted: 4 December 2024

Published online: 12 February 2025



Check for updates

R. O. Parke Loyd^{1⊠}, Ethan Schreyer², James E. Owen², James G. Rogers³, Madelyn I. Broome⁴, Evgenya L. Shkolnik⁵, Ruth Murray-Clay⁴, David J. Wilson⁶, Sarah Peacock^{7,8}, Johanna Teske^{9,10}, Hilke E. Schlichting¹¹, Girish M. Duvvuri^{6,12,13}, Allison Youngblood^{6,8}, P. Christian Schneider¹⁴, Kevin France^{6,13,15}, Steven Giacalone¹⁶, Natasha E. Batalha¹⁷, Adam C. Schneider¹⁸, Isabella Longo⁶, Travis Barman¹⁹ & David R. Ardila²⁰

Exoplanet surveys have shown a class of abundant exoplanets smaller than Neptune on close, <100-day orbits¹⁻⁴. These planets form two populations separated by a natural division at about 1.8 R_{\oplus} termed the radius valley. It is uncertain whether these populations arose from separate dry versus water-rich formation channels, evolved apart because of long-term atmospheric loss or a combination of both⁵⁻¹⁴. Here we report observations of ongoing hydrogen loss from two sibling planets, TOI-776 b $(1.85 \pm 0.13 \, R_{\oplus})$ and TOI-776 c $(2.02 \pm 0.14 \, R_{\oplus})$, the sizes of which near the radius valley and mature (1-4 Gyr) age make them valuable for investigating the origins of the divided population of which they are a part. During the transits of these planets, absorption appeared against the Lyman- α emission of the host star, compatible with hydrogen escape at rates equivalent to 0.03-0.6% and 0.1-0.9% of the total mass per billion years of each planet, respectively. Observations of the outer planet, TOI-776 c, are incompatible with an outflow of dissociated steam, suggesting both it and its inner sibling formed in a dry environment. These observations support the strong role of hydrogen loss in the evolution of closeorbiting sub-Neptunes^{5-8,15,16}.

The planets TOI-776 b and TOI-776 c have bulk densities that allow for degenerate compositions, from half water, half iron-silicate 'water worlds' to dry rocky bodies inflated by hydrogen-helium envelopes¹⁷. TOI-776 b is a keystone planet, demographically located between differing predictions of the location of the radius valley in the radiusperiod plane made from competing formation-evolution models¹⁸. The planets are hosted by a star roughly half the mass of the Sun (spectral type M1V) at a distance of 27 pc from Earth that rotates with a period of $34.4^{+1.4}_{-2.0}$ days, from which we estimate an age of 1-4 Gyr (refs. 17,19-21). They orbit at distances yielding zero-albedo equilibrium temperatures of 514 \pm 17 K and 415 \pm 14 K and are subject to X-ray and extreme ultraviolet (XUV; 100-912.7 Å) irradiation several hundred times that experienced by present-day Earth, based on our estimate of a stellar XUV luminosity near 10^{28} erg s⁻¹ (ref. 17) (see 'Lyman- α and XUV' in Methods and Extended Data Fig. 1). Extended Data Fig. 2 places the planets in the context of the sub-Neptune population and the adjacent population of smaller, denser super-Earths. More system properties are available in Extended Data Table 1.

Hydrogen absorption signal

Observations of the transits of TOI-776 b and c in the Lyman- α line of hydrogen were made in 2021 and 2022 with the Space Telescope Imaging Spectrograph (STIS) of the Hubble Space Telescope (HST). These observations originate from two independent programmes, with differences in instrument configuration ('Data' in Methods). The first programme observed the Lyman-α transit of TOI-776 b in June 2021 with a spectral resolving power of $R \approx 10,000$. The second programme, a stellar characterization campaign, serendipitously captured the transit of TOI-776 b in June 2022 at $R \approx 10,000$ and TOI-776 c in December 2022 at a lower resolving power of $R \approx 1,000$.

Transit absorption appeared in all observations (Fig. 1 and Extended Data Fig. 3). During the observations of the transit of TOI-776 b, flux in the $-37 \,\mathrm{km}\,\mathrm{s}^{-1}$ to $69 \,\mathrm{km}\,\mathrm{s}^{-1}$ velocity range dropped by 2.4σ in both June 2021 and June 2022. Meanwhile, flux in the 100-250 km s⁻¹ reference range did not significantly vary ('Throughput stability' in Methods). During the observations of the transit of TOI-776 c in December 2022,

Eureka Scientific, Oakland, CA, USA, 2 Imperial Astrophysics, Department of Physics, Imperial College London, London, UK, 3 Institute of Astronomy, University of Cambridge, Cambridge, UK, ⁴Department of Astronomy and Astrophysics, University of California, Santa Cruz, CA, USA, ⁵School of Earth and Space Exploration, Arizona State University, Tempe, AZ, USA, ⁶Laboratory for Atmospheric and Space Physics, University of Colorado, Boulder, CO, USA. ⁷University of Maryland Baltimore County, Baltimore, MD, USA. ⁸NASA Goddard Space Flight Center, Greenbelt, MD, USA. 9Earth and Planets Laboratory, Carnegie Institution for Science, Washington DC, USA. 10The Observatories of the Carnegie Institution for Science, Pasadena, CA, USA. 11Department of Earth, Planetary, and Space Sciences, University of California, Los Angeles, CA, USA. 12 Department of Physics and Astronomy, Vanderbilt University, Nashville, TN, USA. 13 Center for Astrophysics and Space Astronomy, University of Colorado, Boulder, CO, USA. ¹⁴Hamburger Sternwarte, Hamburg, Germany. ¹⁵Department of Astrophysical and Planetary Sciences, University of Colorado, Boulder, CO, USA. 16 Department of Astronomy, California Institute of Technology, Pasadena, CA, USA. 17 NASA Ames Research Center. Moffett Field. CA. USA. 18 United States Naval Observatory. Flagstaff Station, Flagstaff, AZ, USA. 19Lunar and Planetary Laboratory, University of Arizona, Tucson, AZ, USA. 20 Jet Propulsion Laboratory, California Institute of Technology, Pasadena, CA, USA. [™]e-mail: astroparke@gmail.com

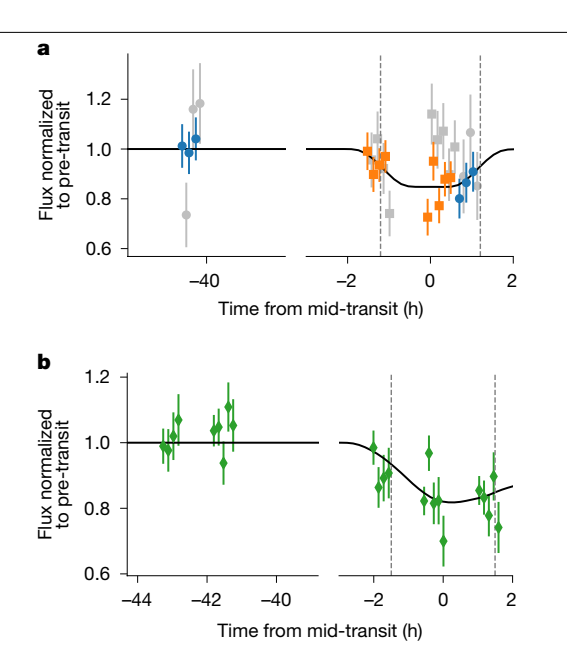


Fig. 1 | Lyman-α transit lightcurves. a, TOI-776 b. b, TOI-776 c. The blue points show data from June 2021, orange squares from June 2022 and green diamonds from December 2022 with 1σ error bars. The black lines are the transits simulated with the median outflow model. The grey background points, slightly offset in time for visual clarity, show flux in a reference 100-250 km s⁻¹ band (not available for TOI-776 c data). The dashed grey lines are the first and last contact points of the optical transit.

Lyman-α flux, integrated over the full line due to low resolution, dropped by 6.7σ .

We estimated the false alarm probability of these signals accounting for key sources of systematic noise using a minimal-parameter model

('Signal significance' in Methods and Extended Data Fig. 3). Fits to the data vielded transit depths of 16.0 \pm 5.4% for TOI-776 b in the -37 km s⁻¹ to 69 km s $^{-1}$ range and 18.7 \pm 3.2% for TOI-776 c over the full line, corresponding to $74^{+11}_{-14}\%$ and $47 \pm 4\%$ of the nominal Hill radius of each planet. For TOI-776 b. identical fits to noise-only lightcurves incorporating systematic wavelength errors yielded a false alarm probability of 0.07%. For TOI-776 c, the strongest possible source of a spurious signal was stellar variability. We addressed this by correlating randomly drawn Lyman-α fluxes with other available stellar emission lines, yielding a maximum false alarm probability of 0.2% (Extended Data Fig. 4).

A limitation of the June 2021 and December 2022 observations is a gap of about 40 h between baseline and transit measurements. This gap introduces vulnerability to false positives from stellar variability, as variations on this timescale are not probed by any existing Lyman-α observations of TOI-776. A transit interpretation of the signals is supported by several lines of evidence: the star rotates only around 5% in 40 h; variations in reference band flux (TOI-776 b) or correlations with activity-tracing lines (TOI-776 c) do not explain the transit signal; for TOI-776 b, a similar transit signal appeared in two observations a year apart. Further observations are needed to fully confirm this interpretation and are likely to occur in 2025 (programme HST-GO-17801).

Atmospheric mass loss

The Lyman-α transit observations can be explained by outflows of hydrogen escaping the planets at rates of $10^{8.3}$ – $10^{9.7}$ g s⁻¹ (TOI-776 b) and $10^{9.0}$ – $10^{9.9}$ g s⁻¹ (TOI-776 c). We obtained these estimates by forward modelling of the transits assuming hydrodynamic outflows funnelled into cometary tails²² ('Outflow model' in Method). The median model is shown in comparison with transit data in Fig. 1 and posteriors on the mass loss rates of hydrogen are shown in Fig. 2. Attempting to match the Lyman-α transit depths without an outflow yields unstable

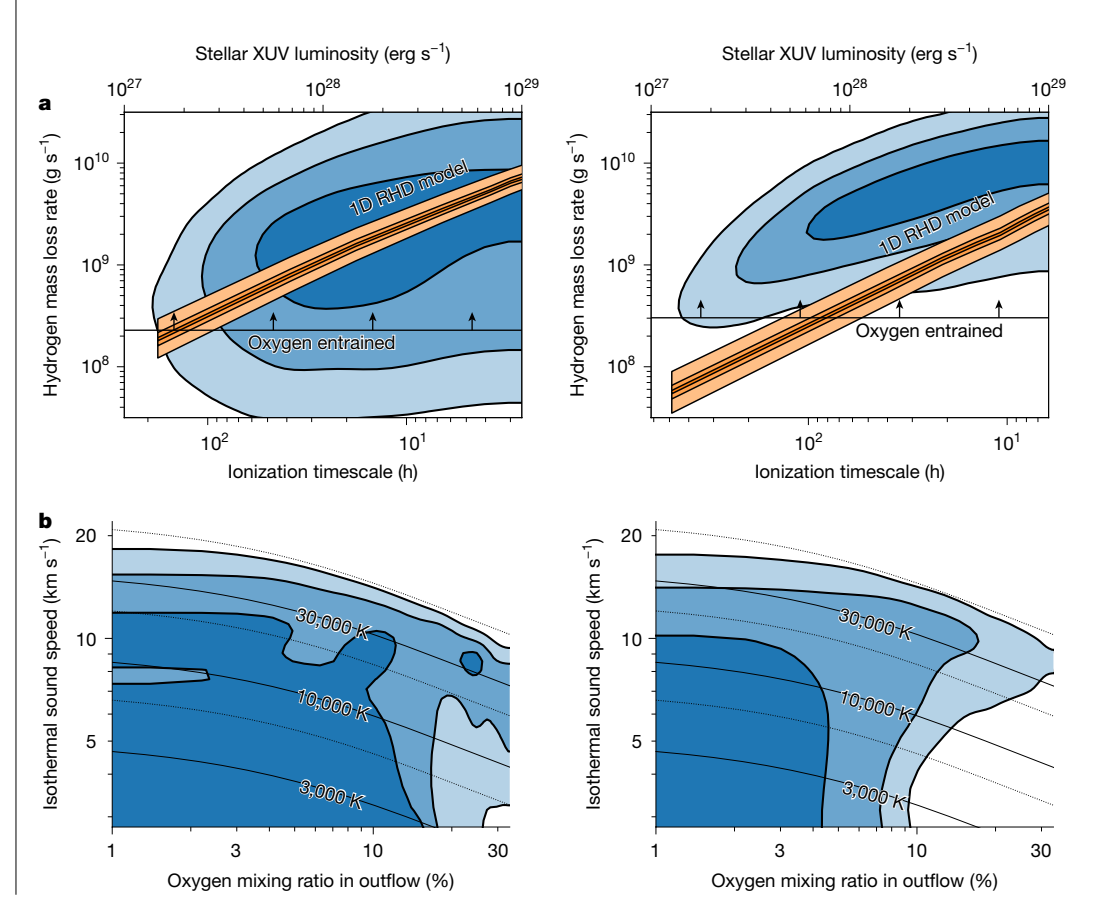


Fig. 2 | Mass loss constraints.

a,b, Left: TOI-776 b. Right: TOI-776 c. The rounded blue contours represent posteriors from the outflow model fits to the Lyman-α transits, enclosing 39.3%, 77.7% and 95% of the posterior probability. a, The blue posteriors are from fits assuming no oxygen. The top axes give the stellar X-ray and XUV luminosity corresponding to the ionization timescales shown on the bottom axes. The linear orange contours represent predictions from a one-dimensional (1D) RHD model broadened by mass and radius uncertainties. The horizontal lines with arrows represent the mass loss rate beyond which atomic oxygen would be dragged into the outflow. **b**, The blue posteriors are from fits, including oxygen as a free parameter. Curves of constant temperature are shown for either a fully neutral gas (solid) or fully ionized plasma (dotted).

solutions unless the planets harbour approximately 100 G magnetic fields (approximately 10× that of Jupiter) to resist a global outflow ('Static atmosphere' in Methods). It is unclear whether these fields are plausible. In population-evolution models, confining fields require lower-density core compositions to match the present radius vallev²³.

For context, other planets with detected Lyman-α transits have estimated rates of hydrogen loss ranging from $10^{8.4}$ g s⁻¹ (the $4.2 R_{\oplus}$ warm-Neptune GJ 436 b) to about 10^{11} g s⁻¹ (for example, the 15.23 R_{\odot} hot-Jupiter HD 209458 b) (refs. 24–26). For TOI-776 b and c, our results indicate that the planets would lose, in hydrogen alone, 0.03–0.6% (TOI-776 b) and 0.1-0.9% (TOI-776 c) of their total mass over the next billion years if loss rates stayed constant. The evolutionary significance of this mass loss is comparable to the hot Neptune GJ 3470 b and warm sub-Neptune HD 63433 c (refs. 27.28). Several other sub-Neptunes have also been observed to be losing hydrogen or helium^{29,30}. Among this group, TOI-776 b and c are remarkable for their combination of sizes near the radius valley and age ≥1 Gyr.

The hydrogen loss rates of TOI-776 b and c can be explained by heating from XUV radiation if their atmospheres are hydrogen-rich. Mass loss rates predicted ab initio from radiative-hydrodynamic (RHD) simulations of solar-metallicity atmospheres ('RHD simulations' in Methods) intersect with the values we estimated a posteriori from fits to the Lyman- α transits (Fig. 2). Core-powered mass loss is not viable because of the low equilibrium temperatures of TOI-776 b and c, yielding mass loss rates of orders of magnitude too low to explain the Lyman- α transits^{7,8}.

Implications for formation and evolution

A hydrogen outflow from the atmosphere of TOI-776 c has implications for its water content and associated formation history. Any oxygen dissociated from the water will be dragged along with the hydrogen outflow given its strength^{31,32} (Fig. 2b and 'Oxygen drag' in Methods). However, oxygen at mixing ratios above about 10% in the outflow of TOI-776 c requires unphysically high temperatures to match the transit data^{33,34} (Fig. 2d). Assuming all oxygen is sourced from dissociated steam, this limits the water content of a mixed steam-hydrogen atmosphere to under 20%, posing a challenge to scenarios in which sub-Neptunes, particularly those with sizes near the radius valley, are dominantly water-rich. In a population model combining water-rich formation with atmospheric escape to match the radius valley. <2% of sub-Neptunes near the radius valley $(1.7-2.4 R_{\odot})$ are as dry as our constraint for TOI-776 c (ref. 14). Our constraint for TOI-776 c adds to early indications that the atmospheric compositions of these planets may vary substantially, contrasting with the >30% mixing ratio of atmospheric water found for the small sub-Neptune GJ 9827 d (1.98 \pm 0.11 R_{\oplus} , $3.02 \pm 0.58 M_{\odot}$, $675 \pm 13 \text{ K}$) (ref. 35).

Formation arguments imply that TOI-776 b is probably no wetter than TOI-776 c. Models indicate that water content generally increases with formation distance from the star, with higher water contents corresponding to more massive planets³⁶. Because TOI-776 b is neither farther from the star nor more massive than TOI-776 c, we conclude it probably formed similarly water-poor. However, the present observations do not enable a direct constraint.

The ensemble of evolutionary tracks in Fig. 3 shows how hydrogen loss has and will continue to substantially alter the atmospheres of TOI-776 b and c. These tracks, generated from a model that successfully reproduces the radius valley, are consistent with the current properties of the planets, including their rates of hydrogen loss 13,37 ('Evolutionary tracks' in Methods). They indicate that TOI-776 b and c formed with hydrogen-helium envelopes making up 1.4-31% (TOI-776 b) and 1.0-24% (TOI-776 c) of their total mass, subsequently lost 84-99% and 62-98% of these envelopes, and presently harbour envelope mass fractions of 0.09-0.6% and 0.16-1.0%, respectively. The remainder of their envelopes are lost in 60% and 47%, respectively,

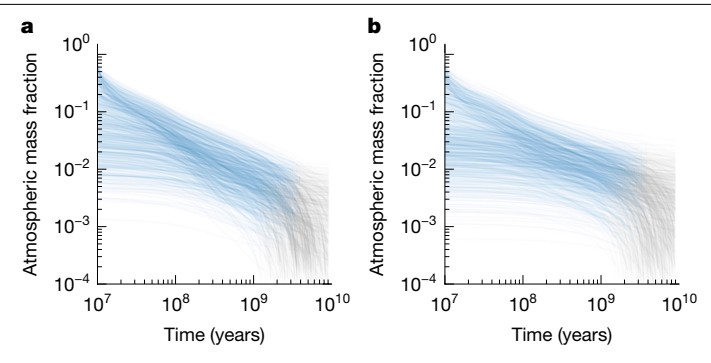


Fig. 3 | Atmospheric evolution of TOI-776 b and c. a, TOI-776 b. b, TOI-776 c. The thin curves represent a modelled ensemble of evolutionary tracks of XUV-driven mass loss consistent with the posteriors on the current system properties. The curves transition from blue to grey when they pass the age, randomly drawn from within the plausible age range of TOI-776, at which the planet was assumed to be observed on each track.

of ensemble tracks before the system age reaches 10 Gyr. In these scenarios, the planets cross the radius valley, becoming super-Earths as their $1.46^{+0.05}_{-0.06}R_{\oplus}$ (TOI-776 b) and $1.55^{+0.08}_{-0.09}R_{\oplus}$ (TOI-776 c) interiors are exposed. Many super-Earths may simply be analogues of TOI-776 b and c that have already completed this transition, consistent with a picture in which both sub-Neptunes and super-Earths formed from an initially unbroken population divided into two through billions of years of atmospheric loss.

Online content

Any methods, additional references, Nature Portfolio reporting summaries, source data, extended data, supplementary information, acknowledgements, peer review information; details of author contributions and competing interests; and statements of data and code availability are available at https://doi.org/10.1038/s41586-024-08490-x.

- Howard, A. W. et al. Planet occurrence within 0.25 AU of solar-type stars from Kepler. Astrophys. J. Suppl. Ser. 201, 15 (2012).
- Dong, S. & Zhu, Z. Fast rise of "Neptune-size" planets (4–8 R_{\oplus}) from $P\sim$ 10 to \sim 250 days statistics of Kepler planet candidates up to ~0.75 AU. Astrophys. J. 778, 53 (2013).
- Fressin, F. et al. The false positive rate of Kepler and the occurrence of planets. Astrophys. J.
- Kunimoto, M., Winn, J., Ricker, G. R. & Vanderspek, R. K. Predicting the exoplanet yield of the TESS Prime and extended missions through years 1-7. Astrophys. J. 163, 290
- Owen, J. E. & Wu, Y. Kepler planets: a tale of evaporation. Astrophys. J. 775, 105 (2013).
- Lopez, E. D. & Fortney, J. J. The role of core mass in controlling evaporation: the Kepler radius distribution and the Kepler-36 density dichotomy. Astrophys. J. 776, 2 (2013).
- Ginzburg, S., Schlichting, H. E. & Sari, R. Core-powered mass-loss and the radius distribution of small exoplanets, Mon. Not. R. Astron. Soc. 476, 759-765 (2018).
- Gupta, A. & Schlichting, H. E. Sculpting the valley in the radius distribution of small exoplanets as a by-product of planet formation: the core-powered mass-loss mechanism. Mon. Not. R. Astron. Soc. 487, 24-33 (2019)
- Zeng, L. et al. Growth model interpretation of planet size distribution, Proc. Natl Acad. Sci. USA 116, 9723-9728 (2019).
- Lee, E. J. & Connors, N. J. Primordial radius gap and potentially broad core mass distributions of super-Earths and sub-Neptunes. Astrophys. J. 908, 32 (2021).
- Bean, J. L., Raymond, S. N. & Owen, J. E. The nature and origins of sub-Neptune size planets. J. Geophys. Res. Planets 126, e2020JE006639 (2021).
- Luque, R. & Pallé, E. Density, not radius, separates rocky and water-rich small planets orbiting M dwarf stars. Science 377, 1211-1214 (2022).
- Rogers, J. G., Schlichting, H. E. & Owen, J. E. Conclusive evidence for a population of water worlds around M dwarfs remains elusive. Astrophys. J. Lett. 947, 19 (2023)
- Burn, R. et al. A radius valley between migrated steam worlds and evaporated rocky cores. Nat. Astron. 8, 463-471 (2024).
- Lecavelier des Etangs, A. A diagram to determine the evaporation status of extrasolar planets. Astron. Astrophys. 461, 1185-1193 (2007).
- Owen, J. E. & Jackson, A. P. Planetary evaporation by UV and X-ray radiation; basic hydrodynamics. Mon. Not. R. Astron. Soc. 425, 2931-2947 (2012).
- Luque, R. et al. A planetary system with two transiting mini-Neptunes near the radius valley transition around the bright M dwarf TOI-776. Astron. Astrophys. 645, A41 (2021).
- Cloutier, R. & Menou, K. Evolution of the radius valley around low-mass stars from Kepler and K2. Astron. J. 159, 211 (2020).

- Angus, R. et al. Exploring the evolution of stellar rotation using galactic kinematics. Astron. J. 160, 90 (2020).
- 20. Engle, S. G. & Guinan, E. F. Living with a red dwarf: the rotation-age relationship of M dwarfs. Astrophys. J. Lett. 954, 50 (2023).
- Lu, Y., Angus, R., Foreman-Mackey, D. & Hattori, S. In this day and age: an empirical gyrochronology relation for partially and fully convective single field stars. Astron. J. 167,
- 22. Schreyer, E., Owen, J. E., Loyd, R. O. P. & Murray-Clay, R. Using Lyman-a transits to constrain models of atmospheric escape. Mon. Not. R. Astron. Soc. 533, 3296-3311 (2024).
- Owen, J. E. & Adams, F. C. Effects of magnetic fields on the location of the evaporation valley for low-mass exoplanets. Mon. Not. R. Astron. Soc. 490, 15-20 (2019).
- 24. Vidal-Madjar, A. et al. An extended upper atmosphere around the extrasolar planet HD209458b. Nature 422, 143-146 (2003).
- 25. Bourrier, V. & Lecavelier des Etangs, A. 3D model of hydrogen atmospheric escape from $\mbox{HD\,209458b}$ and $\mbox{HD\,189733b}$: radiative blow-out and stellar wind interactions. Astron. Astrophys. 557, A124 (2013).
- Kislvakova, K. G. et al. Transit Lyman-a signatures of terrestrial planets in the habitable 26. zones of M dwarfs. Astron. Astrophys. 623, A131 (2019).
- Bourrier, V. et al. Hubble PanCET: an extended upper atmosphere of neutral hydrogen 27. around the warm Neptune GJ 3470b. Astron. Astrophys. 620, A147 (2018).
- 28 Zhang, M. et al. Detection of ongoing mass loss from HD 63433c, a young mini-Neptune. Astron. J 163, 68 (2022).
- 29 Zhang, M. et al. Detection of atmospheric escape from four young mini-Neptunes. Astron. J 165, 62 (2023).
- 30 Zhang, M., Dai, F., Bean, J. L., Knutson, H. A. & Rescigno, F. Outflowing helium from a mature mini-Neptune. Astrophys. J. Lett. 953, 25 (2023).

- Zahnle, K. J. & Kasting, J. F. Mass fractionation during transonic escape and implications for loss of water from Mars and Venus. Icarus 68, 462-480 (1986)
- 32. Hunten, D. M., Pepin, R. O. & Walker, J. C. G. Mass fractionation in hydrodynamic escape. Icarus 69, 532-549 (1987).
- 33. Murray-Clay, R. A., Chiang, E. I., & Murray, N. Atmospheric escape from hot Jupiters. Astrophys. J. 693, 23-42 (2009).
- 34. García Muñoz, A. et al. A heavy molecular weight atmosphere for the super-Earth π Men c. Astrophys. J. 907, L36 (2021).
- 35. Piaulet-Ghorayeb, C. et al. JWST/NIRISS reveals the water-rich "steam world" atmosphere of GJ 9827 d. Astrophys. J. 974, L10 (2024).
- Venturini, J., Guilera, O. M., Haldemann, J., Ronco, M. P. & Mordasini, C. The nature of the radius valley. Hints from formation and evolution models. Astron. Astrophys. 643, L1 (2020).
- Rogers, J. G., Gupta, A., Owen, J. E. & Schlichting, H. E. Photoevaporation versus corepowered mass-loss: model comparison with the 3D radius gap. Mon. Not. R. Astron. Soc. **508**, 5886 (2021).

Publisher's note Springer Nature remains neutral with regard to jurisdictional claims in published maps and institutional affiliations.

Springer Nature or its licensor (e.g. a society or other partner) holds exclusive rights to this article under a publishing agreement with the author(s) or other rightsholder(s); author self-archiving of the accepted manuscript version of this article is solely governed by the terms of such publishing agreement and applicable law.

© The Author(s), under exclusive licence to Springer Nature Limited 2025

Methods

Observations and data reduction

The TOI-776 Lyman- α observations were collected as part of HST programmes 16456 (principal investigator R.O.P.L.) and 16701 (principal investigator A.Y.) using the STIS with the G140M and G140L gratings. Extended Data Table 2 summarizes the observations. The two independent teams that planned these observations chose different slit widths for the observations, 0.05″ (16456) and 0.2″ (16701), which has implications discussed later in this section. One observation, sampling at 0.87 h relative to the transit of planet b, is near the transit of planet c (–3.75 h). However, this exposure avoids the ingress of planet c according to our outflow model fits, implying that the measurement of the transit of planet b is not biased. Observing notes indicate possible guide star acquisition issues during the 2022 G140M observations. We checked for variations in the telescope position angle indicative of pointing drifts and found none.

We used standard pipeline tools (calSTIS) to process the data³⁸. We manually identified the spectral trace in each exposure and forced data extraction at that location. Reference files were those current as of 6 March 2023 retrieved using the Calibration Reference Data System of HST. We used an extraction width (extrsize) of 19 pixels for the G140M data and 13 pixels for the G140L data and background offsets (bkloffst and bk2offst) of ±30 pixels with 20 pixel background widths (bk1size and bk2size). Backgrounds were not smoothed, in contrast with the pipeline default, to avoid leakage of geocoronal airglow that otherwise appeared in the G140L data. The dark subtraction step was omitted because dark count rates were overestimated by the standard pipeline, resulting in nonphysical negative background rates in areas of low flux. The default pipeline wavelength calibration was used, based on emission lines in calibration exposures of the onboard Pt-Cr/Ne lamp taken either immediately before or after each science exposure³⁹. We divided each full exposure into several subexposures with durations of approximately 500 s, with minor adjustments to ensure full use of the total exposure time.

At the time of writing, the stistools.inttag routine used to split exposures into subexposures contained a bug resulting in inaccurately large values in error arrays (J. Lothringer, STScI, personal communication). As a workaround, we deleted the error arrays in the _raw image files following runs of inttag, forcing the pipeline to recompute error arrays during spectral extraction. When fitting the Lyman- α profile and planetary outflow model (see 'Lyman- α and XUV' section), we used Poisson uncertainties based on predicted count rates from the models themselves.

The extracted data and absorption signals proved robust against a range of reduction choices. Variations in lightcurves remained within error bars in response to changes to the size of the extraction region and the location and size of the background regions, the omission or inclusion of background smoothing, and the omission or inclusion of the dark subtraction step. We inspected potential outliers in the Lyman- α transit and pre-transit lightcurves present in some reductions and found them unlikely to be the result of flares or background artefacts or strongly incompatible with Poisson noise. As these points did not drive model fits, we retained all data.

For the TOI-776 b observations, we used differenced in- and out-of-transit spectra, binned to the velocity grid of the 2022 epoch, to identify the velocity range in which absorption was present to be $-37~km~s^{-1}$ to $69~km~s^{-1}$. Choosing a different range would affect the signal, and integrating the entire line reduces the transit to a statistically insignificant level by adding noise without enhancing the signal. For TOI-776 c, specific velocity regions cannot be isolated because of the low resolution of the G140L grating. Thus, we integrated the entire line from approximately $-700~km~s^{-1}$ (avoiding Si III 1,206 Å emission) to 1,000 km s $^{-1}$. As would be the case for TOI-776 b, integrating the entire Lyman- α line probably dilutes the transit signal for TOI-776 c, but the larger planetary Hill sphere and slower ionization rate of TOI-776 c

compensate, yielding a greater outflow volume with higher optical depths and enabling viable transit fits for mass loss rates overlapping with those of TOI-776 b (see 'Outflow model' section).

Throughput stability

Throughput variations during exposures with STIS are known to occur because of thermal variations of the focus of HST (often referred to as 'breathing')^{27,40,41}. Variations between exposures have also been observed^{27,41}.

We searched for throughput variations in the observations of the transit of TOI-776 b by examining flux in a reference 100–250 km s $^{-1}$ band, beyond the range in which Lyman- α absorption has been observed for other planets $^{24,27,28,41-44}$ (Extended Data Fig. 5). Fluxes were constant to within 1σ according to a χ^2 test, both as a function of HST orbital phase and linear time.

As a function of the orbital phase, linear and quadratic polynomial fits yielded the lowest values of the Bayesian information criteria ⁴⁵ for the 2021 and 2022 epoch observations, respectively. However, these fits also yielded reduced χ^2 values below unity, suggestive of overfitting. Because of this and the relative unimportance of intra-exposure versus inter-exposure variations to the observed signal, we chose not to detrend the data in the final analysis.

An identical investigation was not possible for the observations of the transit of TOI-776 c because the Lyman- α line is unresolved in those observations (that is, flux in only the $100-250~\text{km s}^{-1}$ band cannot be isolated). However, calibration data indicate 4.5% RMS (root mean square) throughput variations for the 0.2% slit aperture used in the observations of the transit of TOI-776 c, a value roughly $4\times$ smaller than the transit signal⁴⁰.

Lyman-α and XUV

Only the portion of the stellar Lyman- α emission line corresponding to redshifted Doppler velocities was observable. The remainder was absorbed by hydrogen in the interstellar medium (ISM). Reconstructing the intrinsic stellar Lyman- α line without ISM absorption or instrument broadening was necessary to forward model transit-absorbed spectra with our outflow model and for one XUV reconstruction technique.

We fit the spectrum obtained on 4 June 2021, the only spectrum resolving the line without transit absorption, following the process as described in ref. 46 with a single ISM component. Model parameters and their priors are given in Extended Data Table 3. We used the Markov chain Monte Carlo code Zeus to sample the posterior probability distribution of these parameters with 44 walkers sampling to a chain length more than $10\times$ the autocorrelation length 47,48 . Extended Data Fig. 6 shows the results of the fit. Our fit yielded a median intrinsic Lyman- α flux of $8.95^{+3.4}_{-0.24}\times10^{-14}$ erg s $^{-1}$ cm $^{-2}$.

We supplied the ISM-attenuated profile predicted by the maximumlikelihood fit as a fixed input to the outflow model. The outflow model was free to scale this profile up and down using a separate parameter for each epoch during fitting.

We estimated the XUV spectrum of the star using three separate techniques. The simplest method of estimation was an empirical scaling based on the reconstructed Lyman- α flux covering wavelength bins spanning 100–912 Å (the extreme ultraviolet, EUV) 49 . This method yielded an EUV luminosity of 7.5 \times 10 27 erg s $^{-1}$ based on a reconstructed Lyman- α value at 1 AU of 2.8 erg s $^{-1}$ cm $^{-2}$.

The second and third reconstruction techniques relied on far ultraviolet line fluxes measured from the combined G140L spectra. These fluxes, in units of 10^{-16} erg s $^{-1}$ cm $^{-2}$, were: C III blend (1,175 Å) 2.01 ± 0.35, Si III (1,206 Å) 5.79 ± 0.90, N v blend (near 1,240 Å) 2.28 ± 0.14, Si II (12,67 Å) 0.84 ± 0.24, O I blend (near 1,305 Å) 6.18 ± 0.25, C II blend (near 1,335 Å) 9.70 ± 0.21, Si IV doublet (1,394 Å and 14,013 Å) 3.13 ± 0.34, C IV blend (near 1,549 Å) 10.5 ± 0.5 ; C I blend (1,561 Å) 2.00 ± 0.35 , C I blend (near 1,657 Å) 7.34 ± 0.56 and Al II (1,671 Å) 2.26 ± 0.35.

The second reconstruction covers XUV wavelengths from 6 Å to 912 Å and is based on the differential emission measure (DEM) technique described in refs. 50,51. This approach uses atomic data and a simplified plasma model to describe the structure of the stellar upper atmosphere (chromosphere, transition region and corona) as a one-dimensional (1D) function of temperature. The DEM for TOI-776 was constrained by both X-ray data and the far ultraviolet data detailed in the previous paragraph. X-ray data originate from 28 ks of observation by XMM-Newton on 14 December 2022 (Obs. ID 0892000501, principal investigator A.Y.), contemporaneous with the third epoch of G140L data. Data from the PN, MOS1 and MOS2 detectors were used to reconstruct the X-ray spectrum assuming an absorbing hydrogen column density of 5 × 10¹⁹ cm⁻² and solar elemental abundances scaled to the metallicity listed in Extended Data Table 1. We represented the logarithmic form of the DEM as a fifth-order Chebyshev polynomial and used this to predict fluxes in X-ray bands and far ultraviolet lines, with an added hyperparameter describing systematic uncertainty in these fluxes. Emission line parameters were obtained from v.10.0.1 of the CHIANTI atomic database^{52,53}. We sampled the joint posterior likelihood of the model parameters using the Markov Chain Monte Carlo (MCMC) sampler emcee, with 25 chains run to 100 autocorrelation lengths⁵⁴. Apart from line emission, we included continuum emission from hydrogen and helium species as in ref. 51 to predict the EUV spectrum.

The third reconstruction is based on a 1D radiative model of the stellar atmosphere to simulate its spectral emission using a modification of the PHOENIX code ^{55,56}. The code attaches a chromosphere and transition region extending up to 200,000 K with a prescribed temperature structure to an underlying photosphere in radiative–convective equilibrium. For TOI-776, we used the nominal effective temperature, surface gravity and mass provided in Extended Data Table 1 and tailored the temperature structure of the chromosphere and transition region until the far-ultraviolet line fluxes of the output spectrum matched with those provided earlier in this section. Because the model does not include plasma with temperatures above 200,000 K, emission from the stellar corona is absent. Including treatment of this plasma would probably reverse the slope of the spectrum below about 500 Å and could increase the integrated EUV (100–912 Å) flux by a factor of 2 to 3⁵⁷.

The results of all three reconstructions at EUV wavelengths are compared in Extended Data Fig. 1. The predicted EUV spectra vary substantially as a function of wavelength and the minimum and maximum estimates differ by a factor of 7.6 when integrated from 100 Å to 912 Å. The absolute accuracy of these techniques is not well known, and uncertainties are compounded by stellar variability at XUV wavelengths reaching factors of a few on year timescales $^{50,58-60}$. Consequently, we consider XUV luminosities spanning $10^{27}–10^{29}\,\mathrm{erg}\,\mathrm{s}^{-1}$ to be plausible for TOI-776.

Stellar activity

The stability of Lyman- α emission of TOI-776 can be assessed with out-of-transit data, including the June 2021 observing visit with the G140M grating and three later visits with the G140L grating, totalling 5.1 h of cumulative data separated by intervals of several months. Extended Data Fig. 4 plots the integrated Lyman- α flux across all G140L visits, normalized by the global out-of-transit mean.

On long (month–year) timescales, the average flux from each visit probes variability. Relative to the global mean, these averages are $-4.8\pm1.3\%$ in the first visit; $13.2\pm2.2\%$ in the second visit, 0.6 stellar rotations after the first visit, and $-5.6\pm2.2\%$ in the third visit, 5.9 stellar rotations after the first visit (out-of-transit only). In comparison, the transit visit of TOI-776 c began 0.05 stellar rotations after the pre-transit visit began, making flux variations from rotational variability between pre-transit and transit likely to be smaller than the values just quoted.

On shorter, sub-visit timescales, the point scatter (standard deviation) of 5.7% was slightly lower than that of the median uncertainty of 6.2%, indicating no evidence for additional variability due to the

star or instrument on those timescales. A previous study examined the effect of the Lyman- α variability of the Sun on simulated transit measurements and found that it generally did not significantly bias the measurements⁶¹.

Emissions from other far ultraviolet lines can provide an independent measure of variation in stellar activity. The G140L data include detectable emission from Si²⁺, N⁴⁺, Si³⁺ and C³⁺ ions (the N v 1,238 Å, 1,242 Å; Si Iv 1,393 Å, 1,402 Å; and C Iv 1,548 Å, 1,550 Å lines) that are unlikely to produce substantial transit signals if present in the outflow at solar metallicity⁶². However, in the out-of-transit data, these lines are not well correlated with the Lyman- α emission, probably because they do not form cospatially in the stellar atmosphere⁶³. A Pearson correlation test yields r=0.19, P=29% for Si III; r=-0.06, P=75% for N v; r=-0.18, P=33% for Si IV; and r=0.19, P=29% for C IV. To be conservative we conducted false alarm tests introducing correlated noise based on each of these estimates (see the next section).

Additional lines detected in the G140L data include O I 1,305 Å, C II 1,335 Å and He II 1,640 Å. Extended Data Fig. 4 plots these as well. We did not use these lines as activity probes because of the possibility of transit absorption (O I and C II) and low signal-to-noise ratio (He II). C II exhibits a possible transit, but we consider it likely to be a result of the strong correlation between C II and C IV emission (Pearson r = 0.47, P < 0.01%). O I emission is constant within uncertainties, but the data cannot rule out plausible oxygen entrainment in an outflow sourced by a steam atmosphere.

Although the G140M bandpass includes emission from Si III 1,206 Å and N v 1,238 Å, 1,242 Å lines, substantially lower signal-to-noise ratio prevented an analysis equivalent to the above.

Signal significance

To evaluate the likelihood of a false alarm, we first fit lightcurves of the $-37\,\mathrm{km\,s^{-1}}$ to $69\,\mathrm{km\,s^{-1}}$ flux for TOI-776 b and the integrated line flux for TOI-776 c with a function representing the transit of one solid disk in front of another. The minimal parameters required by this simple model are beneficial for false alarm tests as they mitigate overfitting, are easily interpreted and enable rapid computation to fully explore the allowable parameter space. Although the disk-on-disk model does not allow for leading or trailing tails, it is sufficient for false alarm tests given that the data do not sample well beyond the optical transit. Later, when constraining the physical parameters of an outflow matching the transit data, we used a model including an outflow tail (see 'Outflow model' section).

The free parameters of the model are the pre-transit flux and occulting disk radius. For the observations of TOI-776 b, we used separate parameters for the pre-transit flux at each epoch to allow for differences in the band flux resulting from stellar activity changes over their 1-year separation and the use of differing slit apertures. We fixed the impact parameter and transit duration of the planet midpoint to the best-fit values from ref. 17.

Posterior probabilities were sampled using the Zeus MCMC code with eight walkers to a minimum of 1,000 steps and a factor of 100 greater than the autocorrelation length $^{47,48}\!$. Extended Data Fig. 3 shows the results of those fits.

We estimated false alarm probabilities by replacing the data with noise about a constant value. The noise included measurement uncertainty as well as wavelength error as described in the following paragraphs. We found the minimum χ^2 best-fit for 100,000 trials for both planets and determined the fraction that resulted in a best-fit disk radius larger than that found from the actual data.

The *STIS Instrument Handbook* states a wavelength accuracy of 0.5–1.0 pixels, but this represents an absolute accuracy relative to laboratory values for calibration emission lines. The relative accuracy between exposures and visits is the relevant quantity to the present work, but, to our knowledge, this has not been explicitly measured for observations of Lyman- α with the G140M grating. To measure it, we consulted

the HST archive and identified five suitable datasets: programmes 15904, 12681, 16319, 17152 and 8695, initiated by principal investigators B. E. Wood, D. Ehrenreich, M. Zhang, G. Zhou and T. M. Tripp. For each dataset, we determined the wavelength shifts needed to best match a prominent feature in the spectrum across exposures by minimizing the χ^2 difference, as well as the uncertainty in this shift. The scatter in the wavelength shifts over each dataset, in excess of that explicable from flux uncertainties, ranged from 0.02 to 0.2 pixels (1 σ). Shifts between adjacent exposures were generally lower, with a scatter of 0.03–0.13 pixels (1 σ). We conclude that 0.2 pixels is a reasonable estimate for the scatter between exposures from separate visits and 0.1 is reasonable for adjacent exposures in the same visit.

For each simulated lightcurve, we drew random pixel shifts for each pair of exposures from the two epochs of TOI-776 b observations. For the first epoch, for which the exposures were obtained in separate visits, we set σ = 0.2 pixels. For the second, for which the exposures were obtained consecutively in the same visit, we set σ = 0.1 pixels. In each case, we shifted the spectrum from the first exposure by the randomly drawn value and computed the flux in the original integration band. We then adjusted the points representing the second exposure by this amount.

For the G140L data (TOI-776 c), we conducted an additional test correlating random draws of the Lyman- α flux with the observed variability in other emission lines. To do so, we drew each Lyman- α point in a simulated lightcurve from the collapsed univariate distribution that results from substituting the observed flux of the correlated line at that point in the lightcurve into the appropriate bivariate distribution whose parameters are given in the previous section. This incorporated the effect of possible dips in activity near the transit of planet c when drawing random Lyman- α fluxes for the false alarm test as a means of accounting for the possibility of a spurious transit signal due to stellar activity variations. The largest false alarm probability resulted from using C IV 1,548 Å, 1,550 Å emission as the correlate (see the main text).

Background sources, dominated by geocoronal airglow emission, contribute a substantial fraction of the counts in the bandpasses used to measure the planetary transits (Extended Data Table 2). This background shows much larger variability on intra-exposure timescales than the inter-exposure timescales that drive the transit signal (Extended Data Fig. 3). Varying the location and size of regions on the detector used to estimate background count rates did not substantially affect the signal significance. We conclude that the background (airglow) subtraction step of the data reduction is not likely to have produced a spurious transit signal.

Static atmosphere

Previous works have inferred the presence of atmospheric escape from Lyman- α transits based on absorption beyond the planetary escape velocity and transit depths requiring a minimum occulting area larger than the planetary Hill radius 24,41 . For TOI-776 b and c, these arguments are not fully satisfactory. Although the velocity argument may be applied to TOI-776 b, it cannot be applied to TOI-776 c because of the low velocity resolution of the corresponding observations. For both planets, transit depths allow for occulting areas smaller than their Hill radii (see the main text). Hence, we explored whether a static atmosphere (that is, lacking any radial flow) could be constructed that would produce the observed transits.

To do so, we assumed a spherically symmetric, hydrostatic, isothermal atmosphere of pure hydrogen. We set the base of this atmosphere at the optical planetary radius and truncated it at the Hill sphere. The functional form of the scale height accounted for the radial fall-off of the planetary gravity with a correction for the stellar tide. Photoionization was balanced against thermal recombination as in ref. 33. We treated the atmosphere as optically thin to XUV photons throughout, justified by the approximately five orders of magnitude difference in absorption cross-section of hydrogen atoms to XUV photons at 13.6 eV

and Lyman- α photons at line centre, implying that XUV self-shielding becomes important only in regions that are already opaque to Lyman- α . We used the resulting neutral hydrogen density field to compute an absorption profile with natural and thermal broadening integrated across the projected stellar disk at mid-transit.

In search of absorption compatible with the observations, we sampled temperatures of 2,000 K and 10,000 K and stellar XUV luminosities of 10^{27} erg s⁻¹, 10^{28} erg s⁻¹ and 10^{29} erg s⁻¹, then varied the basal pressure until we achieved an approximate match to the transit depths. We then evaluated the resulting atmospheric profiles for stability against hydrodynamic escape based on the Knudsen number (ratio of particle mean free path to the scale height) at points where a gas particle would be thermally unbound (thermal energy equal to gravitational potential) or where the sonic point would settle in a Parker wind. For any combination of parameters producing adequate absorption to explain the observations, the atmosphere is collisional both at the altitude at which it would become thermally unbound and at the would-be sonic point. Were these conditions to exist in reality, a hydrodynamic outflow would ensue.

A magnetic field might be capable of confining an otherwise unbound atmosphere such as the above. We estimated the field strength required for confinement by equating gas thermal pressure to magnetic pressure and extrapolating the field to the planetary surface assuming the radial dependence of a dipole field (r^3). We computed these values from the base to the Hill radius and took the maximum. The necessary surface field strengths varied from 50 G to 300 G for the range of parameters described previously. Although these field strengths are high in comparison with the Earth and Jupiter, we cannot rule out the possibility that an extended, magnetically confined atmosphere is responsible for the observed transits. Note that, in these cases, escape at 1–10% of the unconfined rates would still be expected to occur through polar openings⁶⁴.

Outflow model

The outflow model simulates Lyman-α transits using a technique designed for efficient computation to enable a thorough exploration of the parameters of the planet, its outflow and the stellar environment that shapes a Lyman- α transit, as detailed in ref. 22. The model splits the outflow into two components. Inside the Hill sphere, it treats the outflow as a spherically symmetric Parker wind, parametrized by a constant mass loss rate and sound speed. The ionization structure of the outflow in this region is calculated using the optically thick ionization equation. Outside the Hill sphere, where the outflow is sculpted into a cometary tail by the stellar tidal field and stellar wind ram pressure, the model treats the outflow as a stream bundle with varying elliptical cross-section. This geometry agrees with the results from three-dimensional hydrodynamic simulations 65-73. Radiation pressure is neglected⁶⁸. The model calculates the trajectory of the tail by assuming a generalized geostrophic balance and the ionization state in the tail using the optically thin ionization equation.

Free parameters for each planet include the mass loss rate, outflow sound speed, tail launch angle (measured relative to the planetary orbital velocity vector) and planet mass. Free parameters for the host star include the XUV luminosity, stellar wind speed and stellar wind mass loss rate. Extended Data Table 4 lists the priors adopted for each parameter. Notably, we imposed a physical prior on the mass loss efficiency, ε , based on an equation for energy-limited mass loss

$$\dot{M} = \epsilon \frac{\pi R_{\rm p}^3 F_{\rm XUV}}{GM_{\rm p}},$$

where R_p and M_p are the planet radius and mass and F_{XUV} is the XUV flux at the planet. In this formulation, ϵ encapsulates the radius at which XUV radiation is absorbed, tidal corrections and the efficiency at which the absorbed energy is converted into work removing mass from the

gravitational potential. Given the possibility of large absorption radii and high efficiencies for small, moderately irradiated planets⁷⁴, as well as uncertainty in the conversion factor for hydrogen ionization between the model and the true XUV spectrum of the star we allowed for a large degree of freedom in ϵ , setting an upper limit of 10.

In a separate model run, we included a parameter specifying the ratio of oxygen to hydrogen for each planet. The effect of oxygen included in the model was to lower the mass loss rate of hydrogen in accordance with its mass fraction.

We fit the transit data of both planets simultaneously, using the precisely measured ratio of their semi-major axes (0.651965 \pm 0.000017; ref. 17) to fix their relative XUV radiation. The stellar wind velocity is expected to be super-Alfvénic at both planets and, therefore, varies logarithmically with distance from the star. We approximated the stellar wind velocity to be the same at both planets, scaling the stellar wind pressure at the planets according to their orbital distances. We assumed a single set of stellar parameters for all observations, following the example of past analyses of the Lyman- α transit of GJ 436 b (refs. 68,75). The similarity of stellar Lyman- α emission between epochs suggests minimal variation in stellar activity (Extended Data Fig. 4). Nonetheless, we advise that any future observations be taken as closely spaced in time as is practically feasible to maximize consistency.

The model assumes all XUV photons have an energy of 20 eV. For an identical XUV luminosity, the spectrum of the star versus the assumption of only 20 eV photons will yield differing hydrogen ionization rates. In Fig. 2a, we used the DEM reconstruction of the XUV spectrum of TOI-776 (see 'Lyman- α and XUV' section) to compute the stellar XUV luminosities (top axis) that would yield the same ionization rates sampled by the model (bottom axis). The DEM spectrum for TOI-776 is substantially harder than the measured solar spectrum, resulting in hydrogen ionization rates several times lower for an equivalent XUV flux.

We additionally fit a version of the model, including charge exchange between stellar wind protons and planetary neutral hydrogen as a process to generate energetic neutral atoms (ENAs), using a fluid description in which these ENAs are generated in a collisional turbulent mixing layer $^{76.77}$. These results did not differ substantially from the model presented here

Extended Data Table 4 provides the 16th–84th percentile ranges of the 95th percentile limits of the posteriors the model inferred for each parameter. Mass loss rate bounds quoted in the main text are the 16th–84th percentiles from the 1D distributions marginalized over all other model parameters. Mismatches between the 16th–84th percentile bounds from the 1D mass loss rate distribution and the extremes of the 39.3% contour intervals in two-dimensional posteriors, including the mass loss rate (Fig. 2a), reflect the non-normality of the posterior.

The upper and lower bounds of the mass loss rate posteriors are driven by the data except the upper bound for TOI-776 c, which reflects a prior we imposed on the mass loss efficiency. The bound is not perfectly sharp in Fig. 2 primarily because of the uncertainty in the planet mass folded into the model. Allowing larger mass loss efficiencies could improve the best-fit χ^2 by up to 3, but do not change the conclusions of this work.

Owing to the limited velocity range of the Lyman- α line that remains after ISM absorption (Extended Data Fig. 6), absorption must come from sources with velocities $\gtrsim\!0$ km s $^{-1}$. As a result, hydrogen still near the velocity of about 10 km s $^{-1}$ at which it is launched from the planet, along with thermal and natural broadening, is responsible for the bulk of the absorption signal in our model. This contrasts with observations of hydrogen loss from GJ 436 b, in which the blue wing of the Lyman- α line is exposed and either ENAs or a wind-deflected outflow tail are thought to produce the observed signal 122,26,68,78,79 .

Moreover, the limited temporal sampling, effectively confined to the optical transit, prevents constraints on the physics of the outflow tail. As a result, model posteriors allow for fits both with and without an extended transit egress. Future observations sampling the transits

through egress would narrow the posteriors of our model, although ISM absorption of blueshifted velocities will remain limiting.

Our model fits enable comparisons of predicted transit signals in velocity ranges for which the transits of other planetary hydrogen outflows have been observed (that is, overcoming the limitations imposed by ISM absorption). In the $-120~\rm km~s^{-1}$ to $-40~\rm km~s^{-1}$ band, for which the transit of approximately 50% of the hydrogen outflow of GJ 436 b has been observed (refs. 41,44), the median model predicts transit depths of 80.2% (TOI-776 b) and 82.7% (TOI-776 c).

Oxygen drag

To estimate the mass loss rate at which oxygen begins to be dragged into the outflow in a hydrogen-dominated atmosphere as well as the rate of diffusion-limited hydrogen escape in an oxygen-dominated atmosphere, we used the diffusion constant for hydrogen and oxygen from ref. 80 and assumed a temperature of T = 5,000 K. The estimated rate varies less than a factor of two for temperatures between 3,000 K and 10,000 K.

RHD simulations

We used a 1D photoionization code adapted from ref. 33 to model the mass loss rates of TOI-776 b and c across a range of XUV luminosities. This code models atmospheric escape as a transonic Parker wind and has been revised to include metals in the planetary atmosphere and their interactions with the XUV spectral irradiance from the host star (M.I.B. et al., manuscript in preparation). For TOI-776, we adopted as the XUV spectrum the DEM reconstruction (see 'Lyman-α and XUV' section), scaled to reproduce the XUV luminosity specified in Fig. 2 across roughly 10 grid points. The atmospheres of TOI-776 b and c were constructed of H, He and O in solar mass fractions (0.7933, 0.2000 and 0.0067, respectively). To approximate the effects of H₃⁺ cooling, which removes a substantial amount of the energy deposited by photons with energies above 70 eV (R. Frelikh et al., manuscript in preparation), we truncated the spectrum in our model at 165 eV and attenuated the flux above 70 eV (17.7 nm) by a factor of 0.7. We simulated the outflow at the substellar point, then multiplied by a factor of 0.3 to scale the result to a global mass loss rate³³. Models were run using the nominal radii and masses for the planets given in Extended Data Table 1. We ran additional models over a grid covering the uncertainties in planetary masses and radii to estimate the corresponding uncertainty envelopes in predicted mass loss rates as shown in Fig. 2. The mass-radius grid for TOI-776 b was incomplete but well-behaved, so we interpolated where necessary.

Evolutionary tracks

We computed evolutionary tracks for two different escape mechanisms, photoevaporation and core-powered mass loss, using the semi-analytic models from refs. 8,81,82. For consistency, we used efficiencies interpolated from the same model described in the previous section, with added grid points to accommodate planetary radii reaching as high as $5\,R_\oplus$ (TOI-776 b) and $6\,R_\oplus$ (TOI-776 c) at young ages. If tracks explored parameters beyond this range, we scaled according to the efficiencies given in ref. 16. We assumed all planet interiors are Earth-like in composition (1/3 iron, 2/3 silicates) with a heat capacity of 10^7 erg g $^{-1}$ K $^{-1}$ (refs. 13,83). The XUV history of the star was assumed to follow the relations in ref. 37, normalized to the present XUV luminosity of TOI-776.

To determine the allowable histories and futures of TOI-776 b and c, we performed 50,000 simulations under each mass loss mechanism for each planet. Time-invariant parameters were randomly drawn from normal distributions with variances set by the published uncertainties: stellar mass, stellar metallicity, planetary orbital period and planet interior mass, taken as equal to the present planet mass given the negligible added mass of a hydrogen-helium envelope. Each model was initialized at 10 Myr with an atmospheric mass fraction (atmospheric

mass/interior mass) drawn log-uniformly between 0.001 and 0.7. The upper limit avoids self-gravitating atmospheres not implemented in the model.

We drew a random stellar age uniformly between 1 Gyr and 4 Gyr to observe the planet. The track was then weighted based on a Gaussian likelihood of the mass loss rate, based on the posterior provided by the outflow model, as well as the planet radius and mass with uncertainties shown in Extended Data Table 1. These weights were then used to redraw a sample of 1,000 tracks from the initial ensemble. The atmospheric mass fractions predicted by these tracks are shown in Fig. 3.

Data availability

The datasets analysed during this study are publicly available in the Mikulski Archive for Space Telescopes at https://doi.org/10.17909/a8ib-3759.

Code availability

The Space Telescope Environment for Python and stistools package used to process the STIS data are publicly available at https://stistools.readthedocs.io/en/latest. Code for data reduction and analysis and for generating all figures and values except those relating to the evolutionary tracks is available on Zenodo at https://doi.org/10.5281/zenodo.13976674 (ref. 84). The outflow model code is publicly available at https://github.com/eschreyer/LyA_code. The code used to generate evolutionary tracks is available at https://github.com/jo276/EvapMass, along with the efficiency interpolator as part of the main code package, and chains from the most recent run are present in the Zenodo archive. A beta release of the RHD code is available at https://github.com/mibroome/wind-ae/.

- 38. Sohn, T. S. STIS Data Handbook v.7 (STScI, 2019).
- 39. Medallon, S. & Welty, D. STIS Instrument Handbook for Cycle 31 v.22.0 (STScI, 2023).
- Bohlin, R. & Hartig, G. Clear aperture fractional transmission for point sources. STIS Instrum Sci. Rep. 98, 20 (1998).
- Ehrenreich, D. et al. A giant comet-like cloud of hydrogen escaping the warm Neptunemass exoplanet GJ 436b. Nature 522, 459–461 (2015).
- Lecavelier des Etangs, A. et al. Evaporation of the planet HD 189733b observed in H I Lyman-a. Astron. Astrophys. 514, A72 (2010).
- Kulow, J. R., France, K., Linsky, J. & Parke Loyd, R. O. LYa transit spectroscopy and the neutral hydrogen tail of the hot Neptune GJ 436b. Astrophys. J. 786, 132 (2014).
- Ben-Jaffel, L. et al. Signatures of strong magnetization and a metal-poor atmosphere for a Neptune-sized exoplanet. Nat Astron 6, 141–153 (2022).
- Liddle, A. R. Information criteria for astrophysical model selection. Mon. Not. R. Astron. Soc. 377, L74–L78 (2007).
- Wilson, D. J. et al. Testing Lya emission-line reconstruction routines at multiple velocities in one system. Astrophys. J. 936, 189 (2022).
- Karamanis, M., Beutler, F. & Peacock, J. A. zeus: a PYTHON implementation of ensemble slice sampling for efficient Bayesian parameter inference. Mon. Not. R. Astron. Soc. 508, 3589–3603 (2021).
- 48. Karamanis, M. & Beutler, F. Ensemble slice sampling. Stat. Comput. 31, 61 (2021).
- Linsky, J. L., Fontenla, J. & France, K. The intrinsic extreme ultraviolet fluxes of F5 V to M5 V stars. Astrophys. J. 780, 61 (2014).
- Duvvuri, G. M. et al. Reconstructing the extreme ultraviolet emission of cool dwarfs using differential emission measure polynomials. Astrophys. J. 913, 40 (2021).
- Feinstein, A. D. et al. AU Microscopii in the far-UV: observations in quiescence, during flares, and implications for AU Mic b and c. Astron. J 164, 110 (2022).
- Dere, K. P., Landi, E., Mason, H. E., Monsignori Fossi, B. C. & Young, P. R. CHIANTI—an atomic database for emission lines. Astron. Astrophys. Suppl. Ser. 125, 149–173 (1997).
- del Zanna, G. & Young, P. R. Atomic data for plasma spectroscopy: the CHIANTI database, improvements and challenges. Atoms 8, 46 (2020).
- Foreman-Mackey, D., Hogg, D. W., Lang, D. & Goodman, J. emcee: the MCMC hammer. Publ. Astron. Soc. Pac. 125, 306 (2013).
- Peacock, S. et al. Predicting the extreme ultraviolet radiation environment of exoplanets around low-mass stars: GJ 832, GJ 176, and GJ 436. Astrophys. J. 886, 77 (2019).
- Peacock, S. et al. HAZMAT VI: the evolution of extreme ultraviolet radiation emitted from early M stars. Astrophys. J. 895, 5 (2020).
- Tilipman, D., Vieytes, M., Linsky, J. L., Buccino, A. P. & France, K. Semiempirical modeling of the atmospheres of the M dwarf exoplanet hosts GJ 832 and GJ 581. Astrophys. J. 909, 61 (2021).
- Johnstone, C. P., Bartel, M. & Güdel, M. The active lives of stars: a complete description of the rotation and XUV evolution of F, G, K, and M dwarfs. Astron. Astrophys. 649, A96 (2021).
- Drake, J. J. et al. NExtUP: the normal-incidence extreme ultraviolet photometer. Proc. SPIE 11821. 1182108 (2021).

- France, K. et al. Extreme-ultraviolet stellar characterization for atmospheric physics and evolution mission: motivation and overview. J. Astron. Telesc. Instrum. Syst. 8, 014006 (2022).
- Llama, J. & Shkolnik, E. L. Transiting the Sun. II. The impact of stellar activity on Lya transits. Astrophys. J. 817, 81 (2016).
- Linssen, D. & Oklopčić, A. Expanding the inventory of spectral lines used to trace atmospheric escape in exoplanets. Astron. Astrophys. 675, 193 (2023).
- Avrett, E. H. & Loeser, R. Models of the solar chromosphere and transition region from SUMER and HRTS observations: formation of the extreme-ultraviolet spectrum of hydrogen, carbon, and oxygen. Astrophys. J. Suppl. Ser. 175, 229–276 (2008).
- Owen, J. E. & Adams, F. C. Magnetically controlled mass-loss from extrasolar planets in close orbits. Mon. Not. R. Astron. Soc. 444, 3761–3779 (2014).
- Bisikalo, D. et al. Three-dimensional gas dynamic simulation of the interaction between the exoplanet WASP-12b and its host star. Astrophys. J. 764, 19 (2013).
- Matsakos, T., Uribe, A. & Königl, A. Classification of magnetized star-planet interactions: bow shocks, tails, and inspiraling flows. Astron. Astrophys. 578, A6 (2015).
- Carroll-Nellenback, J. et al. Hot planetary winds near a star: dynamics, wind-wind interactions, and observational signatures. Mon. Not. R. Astron. Soc. 466, 2458–2473 (2017)
- Khodachenko, M. L. et al. Global 3D hydrodynamic modeling of in-transit Lya absorption of GJ 436b. Astrophys. J. 885, 67 (2019).
- McCann, J., Murray-Clay, R. A., Kratter, K. & Krumholz, M. R. Morphology of hydrodynamic winds: a study of planetary winds in stellar environments. Astrophys. J. 873, 89 (2019).
- Debrecht, A. et al. Effects of radiation pressure on the evaporative wind of HD 209458b. Mon. Not. R. Astron. Soc. 493, 1292–1305 (2020).
- Carolan, S., Vidotto, A. A., Villarreal D'Angelo, C. & Hazra, G. Effects of the stellar wind on the Ly a transit of close-in planets. Mon. Not. R. Astron. Soc. 500, 3382–3393 (2021).
- Hazra, G., Vidotto, A. A., Carolan, S., Villarreal D'Angelo, C. & Manchester, W. The impact of coronal mass ejections and flares on the atmosphere of the hot Jupiter HD189733b. Mon. Not. R. Astron. Soc. 509, 5858–5871 (2022).
- MacLeod, M. & Oklopčić, A. Stellar wind confinement of evaporating exoplanet atmospheres and its signatures in 1083 nm observations. Astrophys. J. 926, 226 (2022).
- Salz, M., Schneider, P. C., Czesla, S. & Schmitt, J. H. M. M. Energy-limited escape revised: the transition from strong planetary winds to stable thermospheres. *Astron. Astrophys.* 585, L2 (2016).
- Lavie, B. et al. The long egress of GJ 436b's giant exosphere. Astron. Astrophys. 605, L7 (2017).
- Tremblin, P. & Chiang, E. Colliding planetary and stellar winds: charge exchange and transit spectroscopy in neutral hydrogen. Mon. Not. R. Astron. Soc. 428, 2565–2576 (2013).
- Debrecht, A. et al. Effects of charge exchange on the evaporative wind of HD 209458b. Mon. Not. R. Astron. Soc. 517, 1724–1736 (2022).
- Bourrier, V., Lecavelier des Etangs, A., Ehrenreich, D., Tanaka, Y. A. & Vidotto, A. A. An evaporating planet in the wind: stellar wind interactions with the radiatively braked exosphere of GJ 436 b. Astron. Astrophys. 591, A121 (2016).
- Villarreal D'Angelo, C., Vidotto, A. A., Esquivel, A., Hazra, G. & Youngblood, A. GJ 436b and the stellar wind interaction: simulations constraints using Lya and Ha transits. Mon. Not. R. Astron. Soc. 501. 4383–4395 (2021).
- Mason, E. A. & Marrero, T. R. in Advances in Atomic and Molecular Physics Vol. 6 (eds Bates, D. R. & Esterman, I.) 155–232 (Elsevier, 1970).
- Owen, J. E. & Wu, Y. The evaporation valley in the Kepler planets. Astrophys. J. 847, 29 (2017).
- Rogers, J. G. & Owen, J. E. Unveiling the planet population at birth. Mon. Not. R. Astron. Soc. 503, 1526–1542 (2021).
- 83. Valencia, D., Ikoma, M., Guillot, T. & Nettelmann, N. Composition and fate of short-period super-Earths: the case of CoRoT-7b. Astron. Astrophys. **516**, A20 (2010).
- Loyd, R. O. Parke. Hydrogen escaping from a pair of exoplanets smaller than Neptune: data analysis code. Zenodo https://doi.org/10.5281/zenodo.13976674 (2024).
- Petigura, E. A. et al. The California-Kepler Survey. X. The radius gap as a function of stellar mass, metallicity, and age. Astron. J. 163, 179 (2022).
- 86. Gaia Collaboration et al. The Gaia mission. Astron. Astrophys. 595, A1 (2016).
- Gaia Collaboration et al. Gaia Data Release 2: summary of the contents and survey properties. Astron. Astrophys. 616, A1 (2018).
- Woods, T. N. et al. Solar EUV Experiment (SEE): mission overview and first results.
 J. Geophys. Res. Space Phys. 110, A01312 (2005).
- Youngblood, A. et al. Intrinsic Lya profiles of high-velocity G, K, and M dwarfs. Astrophys. J. 926, 129 (2022).
- Redfield, S. & Linsky, J. L. The structure of the local interstellar medium. IV. Dynamics, morphology, physical properties, and implications of cloud-cloud interactions. Astrophys. J. 673, 283–314 (2008).
- Linsky, J. L. et al. What is the total deuterium abundance in the local galactic disk? Astrophys. J. 647, 1106–1124 (2006).

Acknowledgements Contributions by R.O.P.L were supported by NASA through programme HST-GO-16456. Additional support for R.O.P.L., M.I.B. and R.M.-C. was provided through programme HST-GO-16731. These programmes are administered through grants from the Space Telescope Science Institute, which is operated by the Associations of Universities for Research in Astronomy, under NASA contract NAS 5-26555. E.S. and J.E.O. received funding from the European Research Council (ERC) under the European Union's Horizon 2020 research and innovation programme (grant agreement number 853022, PEVAP). J.E.O. is supported by a Royal Society University Research Fellowship. Contributions by S.P. were supported by NASA under award number 80GSFC24M0006. R.M.-C. and E.S. acknowledge support from NASA XRP grant 80NSSC23K0282. This research is based on observations made with the NASA/ESA HST, obtained from the Space Telescope Science Institute, which is operated by the Association of Universities for Research in Astronomy, under NASA contract NAS 526555. These observations are associated with programmes 16456 and 16701. We thank R. Burn et al. for sharing detailed results of their formation–evolution model.

Author contributions R.O.P.L. identified targets and planned the observations of HST programme 16456, processed all HST data, reconstructed the Lyman-a profile, estimated the signal significance, wrote scripts to provide fit statistics for the outflow model, created figures and wrote the paper. E.S. conducted outflow modelling, interpreted the origin of the transit signals and drafted the 'Outflow model' section. J.E.O. conducted RHD modelling for the paper and the proposal for 16456, provided input to the paper and advised E.S.; J.G.R. modelled evolutionary tracks for the planets, drafted the 'Evolutionary tracks' section and provided Fig. 3. M.B. conducted RHD modelling of the planets and drafted the 'RHD simulations' section. E.L.S. originated the idea of targeting high radial velocity systems and drafted a first draft of the proposal for programme 16456. E.L.S. and J.T. suggested the observations may have implications for water content. R.O.P.L., J.E.O., R.M.-C., H.E.S., E.S. and J.G.R. jointly interpreted implications for water content and planetary formation and evolution. D.J.W. extracted initial STIS G140L spectra. D.J.W., A.Y., K.F. and J.T. assisted with data analysis and signal verification. S.P. generated the PHOENIX-based XUV reconstruction and drafted the 'Lyman-a and XUV' section. H.E.S. advised J.G.R.; G.M.D. reconstructed an XUV spectrum and drafted the 'Lyman-a and XUV' section. A.Y. identified targets and planned the observations of HST programme 16701. P.C.S. analysed X-ray data for the DEM

XUV reconstruction. S.G. validated TOI-776 b and TOI-776 c as bonafide planets. I.L. measured ultraviolet line fluxes for input to XUV reconstructions. R.O.P.L., J.E.O., R.M.-C., A.C.S., T.B., S.P., S.G. and D.R.A. are members of the proposing team for programme 16456. A.Y., K.F., P.C.S., G.M.D. and D.J.W. are members of the proposing team for programme 16701. J.E.O., E.L.S., P.C.S., J.T., H.E.S., K.F., N.E.B., D.J.W., A.C.S., S.P., M.B., T.B. and D.R.A. provided feedback for the project and the paper.

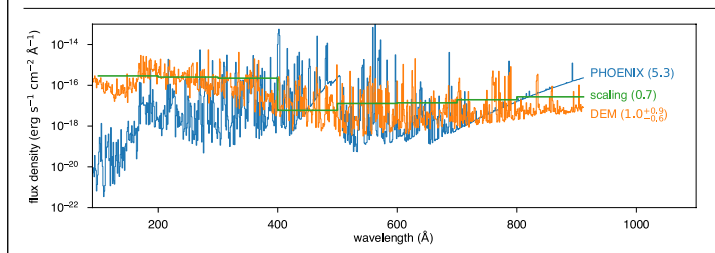
Competing interests The authors declare no competing interests.

Additional information

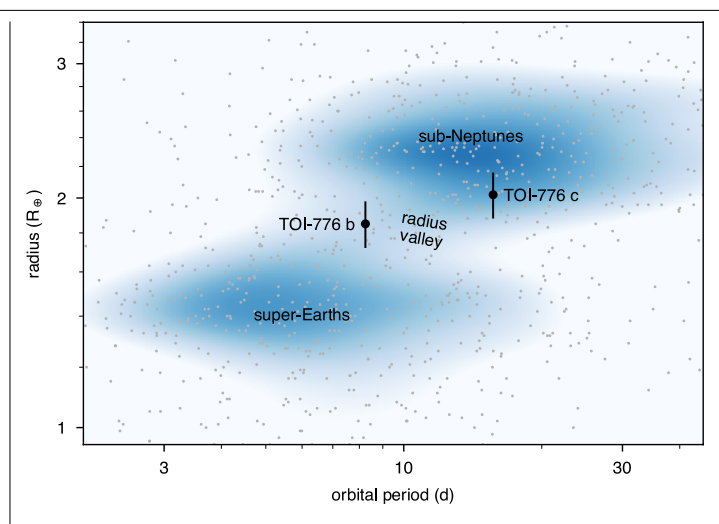
Supplementary information The online version contains supplementary material available at https://doi.org/10.1038/s41586-024-08490-x.

Correspondence and requests for materials should be addressed to R. O. Parke Loyd. Peer review information Nature thanks Alain Lecavelier Etangs and the other, anonymous, reviewer(s) for their contribution to the peer review of this work. Peer reviewer reports are available.

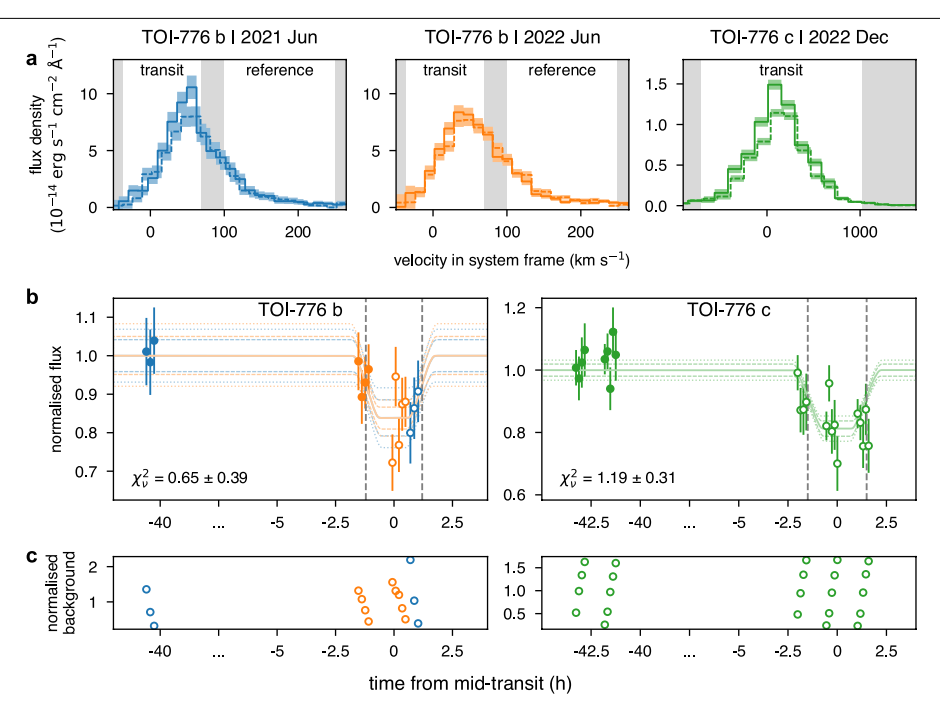
Reprints and permissions information is available at http://www.nature.com/reprints.



Extended Data Fig. 1 | **Reconstructions of the EUV spectrum.** Reconstructions of the intrinsic EUV spectrum of TOI-776 as seen from Earth based on a PHOENIX stellar model (blue), DEM model (orange), and scaling relationship (green) 49,50,51,55,56 . Values in parentheses following the line labels are the luminosity integrated across the range 100-912 Å in units of 10^{28} erg s⁻¹.

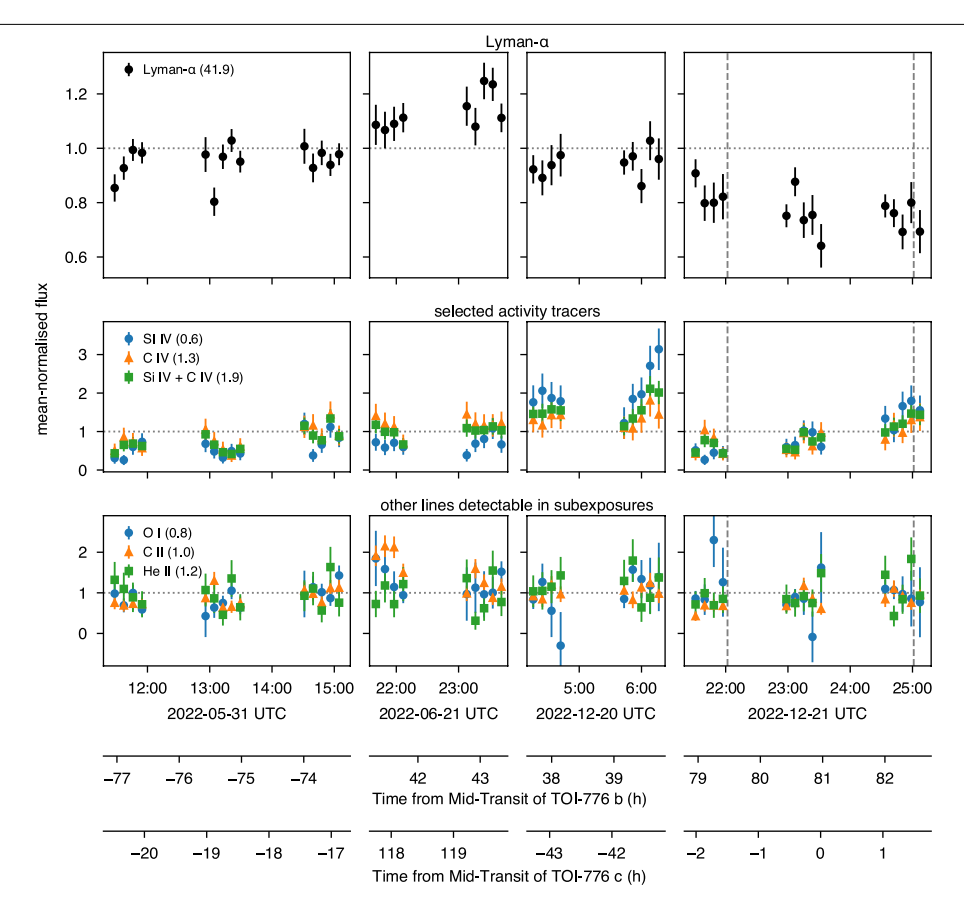


Extended Data Fig. 2 | **Demographic location of TO1-776 b & c.** Black points with error bars are planets TO1-776 b & c, shown in the context of a well-characterised sample of 1246 planets (grey points) from ref. 85 orbiting hosts with effective temperatures (T_{eff}) ranging from 3500 to 6700 K. Shading indicates the relative density of points.



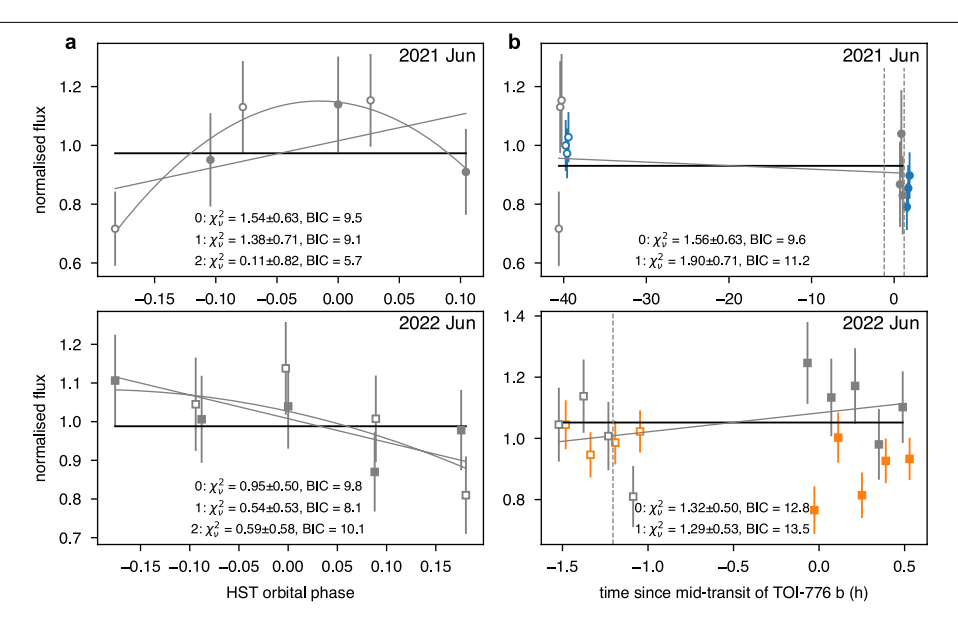
Extended Data Fig. 3 | **Transit spectra and lightcurves. a**, Spectra of the Lyman- α line in and out of transit. Unshaded regions indicate integration bands used to create lightcurves shown in Fig. 1 ('transit') and Extended Data Fig. 4 ('reference'). The selection of these regions is explained in Methods: Data. Colours indicating epoch correspond between Fig. 1, this figure, and Extended Data Fig. 3. Line style represents pre-transit (solid) and transit (dashed). The large difference in flux density and line width between the 2022 Dec and earlier observations is an instrument resolution effect. Envelopes around the lines

are 1 σ uncertainties. **b**, Lightcurves integrated over the bands shown in **a**. Filled and open points correspond to solid and dashed lines in **a**. Lightcurves were fitted with an occulting disk transit to estimate signal significance (solid: best fit, dashed: 68% confidence interval, dotted: 95% confidence interval). Data and curves are normalised by the pre-transit flux from the best fit. **c**, Background count rates in the integrated band, due primarily to geocoronal airglow, normalised by the mean value for each observation epoch.



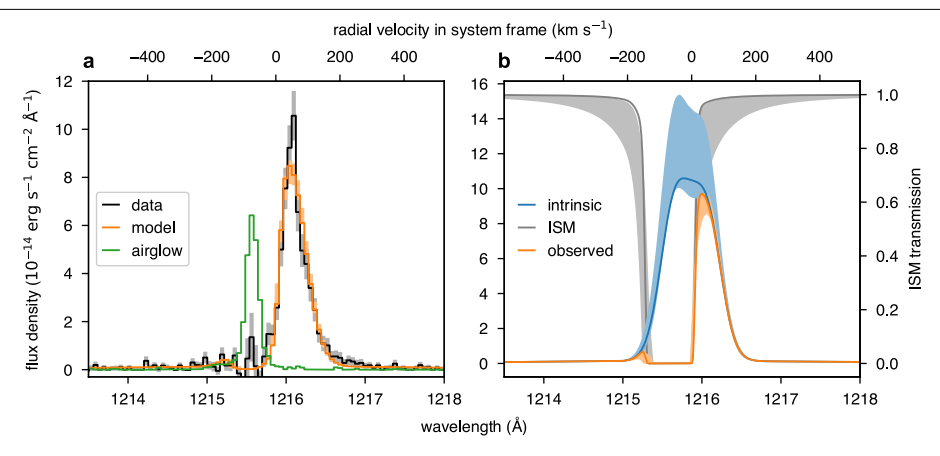
Extended Data Fig. 4 | **Emission line time series.** Lightcurves of integrated line fluxes from all epochs of G140L data. Lyman- α values are normalised to the mean from the first three visits, shown in parenthesis in the rightmost panel in

 $units of 10^{-15} erg \, s^{-1} cm^{-2}. Others are normalised to the global mean, also shown in parenthesis. Dashed grey lines indicate the optical transit of TOI-776 c.$



Extended Data Fig. 5 | **Reference band time series. a**, Lightcurves of Lyman- α flux in the 100–250 km s⁻¹ reference range (grey points) and in the –37–69 km s⁻¹ range (coloured points, offset slightly in time for visual clarity) as a function of HST orbital phase from the 2021 June and 2022 June epochs. **b**, Lightcurves of Lyman- α flux in the 100–250 km s⁻¹ reference range as a function of linear time.

Filled points are from the first exposure and open points are from the second exposure of each epoch. Curves show polynomial fits of order 0,1, and 2 with associated fit statistics shown in each panel, with emphasis on the zeroth-order fit (flat line) to indicate our choice not to detrend the data. Dashed grey lines denote optical ingress and egress.



applied to the signal (green). **b**, Maximum-likelihood model of the intrinsic Lyman- α line (blue), ISM absorption (grey), and absorbed line (orange) with 68% confidence regions (shading). The slight offset of the maximum-likelihood model from the 68% confidence region is due to a nearly flat posterior on the ISM column density over 10^{17} – 10^{18} cm $^{-2}$.

Extended Data Table 1 | Properties of the TOI-776 system

	Host Star				
Designations	TOI-776, LP 961-53, 2MASS J11541839-37330				
Spectral Type	M1V				
Mass	0.544 ± 0.028 M _o				
Radius	0.538 ± 0.024 R _o				
Effective Temperature	3709 ± 70 K				
log ₁₀ Surface Gravity	$4.727 \pm 0.025 \log_{10}(\text{cm s}^{-2})$				
Metallicity, [Fe/H]	-0.20 ± 0.12				
Rotation Period	34. 4 ^{+1.4} _{-2.0} d				
Age	1–4 Gyr				
XUV Luminosity	10 ^{28 ± 1} erg s-1				
Distance	27.17010 ± 0.03205 pc				
Radial Velocity	$49.34 \pm 0.22 \text{ km s}^{-1}$				
	Planets				
Designation	TOI-776 b	TOI-776 c			
Mass	4.0 ± 0.9 M _®	5.3 ± 1.8 M _®			
Radius	$1.85 \pm 0.13 R_{\scriptscriptstyle \odot}$	$2.02 \pm 0.14 R_{\scriptscriptstyle \odot}$			
Equilibrium Temperature	514 ± 17 K	415 ± 14 K			
Instellation	11.5 ± 0.6 S _® 4.9 ± 0.6 S _®				
Orbital Period	8. 24661 ^{+0.0005} _{-0.0004} d 15. 6653 ^{+0.0004} _{-0.0003} d				
Bulk Density	3. $4_{-0.9}^{+1.1}$ g cm ⁻³ 3. $5_{-1.3}^{+1.4}$ g cm ⁻³				
Semi-major Axis	0.0652 ± 0.0015 au 0.1000 ± 0.0024 au				
Incident XUV Flux	10 ^{2.9 ± 1} erg s ⁻¹ cm ⁻²	10 ^{2.6 ± 1} erg s ⁻¹ cm ⁻²			
	$10^{2.5 \pm 1} S_{XUV,\oplus}$	$10^{2.1 \pm 1} S_{XUV,\oplus}$			

Age estimated based on the stellar rotation period via refs. 19–21. Distance from the GAIA observatory 86,87 . See Methods: Lyman-a and XUV for XUV luminosity estimation. Incident XUV flux based on the stellar XUV luminosity and $S_{\text{XUV,B}} \approx 3$ erg s $^{-1}$ cm $^{-2}$ for present-day Earth based on the spectrum of ref. 88. All other properties reproduced from ref. 17.

Extended Data Table 2 | Observing log

UTC Date	Julian Date	Grating	Slit	T_{exp}	$t_{ m b}$	t _c	F_{AG}	V _X	Dataset ID
				(h)	(h)	(h)	(%)	(km s ⁻¹)	
Used to Meas	Used to Measure Transit								
2021-06-04	2459369.653	G140M	0.05	0.50	-40.42	-45.04	4.1 ± 0.5	-29	oei103010
2021-06-05	2459371.373	G140M	0.05	0.50	0.87	-3.75	6.5 ± 0.7	-24	oei104010
2022-06-20	2459750 . 627	G140M	0.2	0.70	-1.30	75.12	22.8 ± 0.9	-11	oeoo16010
2022-06-20	2459750 . 690	G140M	0.2	0.70	0.21	76.64	28.5 ± 1.0	-11	oeoo16020
2022-12-20	2459933.687	G140L	0.2	0.59	37.92	-43.04	64.1 ± 0.9	-	oeoo40010
2022-12-20	2459933.750	G140L	0.2	0.70	39.44	-41.53	59.4 ± 0.8	-	oeoo40020
2022-12-21	2459935.406	G140L	0.2	0.59	79.18	-1.79	66.2 ± 0.9	-	oeoo39010
2022-12-21	2459935.469	G140L	0.2	0.70	80.70	-0.27	64.9 ± 0.9	-	oeoo39020
2022-12-22	2459935 . 535	G140L	0.2	0.70	82.28	1.32	65.1 ± 0.9	-	oeoo39030
Other									
2022-05-31	2459730.987	G140L	0.2	0.59	-76.82	-20.26	29.6 ± 0.6	_	oeoo14010
2022-05-31	2459731.050	G140L	0.2	0.70	-75.30	-18.74	39.1 ± 0.7	_	oeoo14020
2022-05-31	2459731.117	G140L	0.2	0.70	-73.71	-17.15	38.3 ± 0.7	_	oeoo14030
2022-06-21	2459752.412	G140L	0.2	0.59	41.54	117.97	53.8 ± 0.8	_	oeoo15010
2022-06-21	2459752.475	G140L	0.2	0.70	43.06	119.49	54.2 ± 0.7	=	oeoo15020

All time values are given in the barycentric frame. Slit refers to the width of the slit aperture used in arcseconds. Columns t_b and t_c give the time relative to mid-transit for planets b & c at the midpoint of the exposure based on the ephemeris of ref. 17. F_{AC} gives the fraction of the counts within the bandpass used for the transit measurement attributed to airglow and other backgrounds and v_x gives the velocity in the system frame at which the estimated background count rate drops below the signal count rate.

Extended Data Table 3 | Lyman- α line profile fit parameters

Parameter	Units	Priors	Posterior	Notes
Stellar Radial Velocity	km s ⁻¹	N(0, 6.5) & U(-13, 13)	$-6.0_{-3.8}^{+6.4}$	Prior allows for offsets due to error in the instrument wavelength calibration. Quoted values are relative to the star's known 49.34 km s ⁻¹ RV.
				Broad Emission
Flux	10 ⁻¹⁵ erg s ⁻¹ cm ⁻²	U(0, 1000)	8. 0 +0.9 -0.9	
Broadening parameter	km s ⁻¹	$U(0, 1000)$ $b_b > b_n$	756_{-54}^{+88}	
				Narrow Emission
Flux	10 ⁻¹³ erg s ⁻¹ cm ⁻²	U(0, 100)	$1.83^{+0.74}_{-0.12}$	
Broadening parameter	km s ⁻¹	U(0, 1000)	76. $4_{-4.1}^{+4.0}$	
		Central Absorption (Self-Reversal)		
Self-absorption parameter		U(1, 2)	< 1.6	Prior is based on observed values for M stars from ref. 89.
Self-absorption shift	km s ⁻¹	U(0, 0.1b _n)	< 7.17	
		ISM Absorption		
Radial Velocity	km s ⁻¹	U(-40, 20)	$-17.6_{-8.1}^{+5.4}$	Prior is based on predicted radial velocities of ISM clouds near the line of sight that range from -11 to 4 km s ⁻¹ (ref. ⁹⁰).
Log Column Density	log(cm ⁻²)	U(17, 30)	< 18.5	Prior lower limit based on ref. 90 , upper limit was chosen not to be constraining.
Broadening parameter	km s ⁻¹	N(1.06, 0.3) < 3	19. 5 ^{+7.0} _{-8.5}	Prior follows the value assumed by ref. ⁴⁶ , allowing for a factor 2 variance. The upper limit prevents the sampler from becoming stuck on solutions with effectively flat absorption profiles.
Log Deuterium/Hydrogen ratio		N(-4.81,0.25) N(-4.81,0.1)	$-4.86^{+0.12}_{-0.25}$	Prior based on values measured in ref. 91 and represents an asymmetric normal distribution with $\sigma=0.25$ for values < -4.81 and 0.1 for value \geq -4.81.

Uncertainties specify the 16^{th} – 84^{th} confidence interval. U stands for uniform distribution and N for normal distribution. Where the posterior is given as an upper limit, the upper limit is taken as the 95^{th} percentile. The self-reversal parameter, p, is defined as in ref. 89, applied only to the narrow emission component. The Doppler broadening parameter is related to σ in the Gaussian component of the Voigt profiles by $b = \sqrt{2} \, c\sigma/v_0$, where c is the speed of light and v_0 is the frequency at line centre. The following references are cited in this table: refs. 46,89–91.

Extended Data Table 4 | Outflow model parameters

Parameter	Units	Prior	Posterior	Notes
				Star
Log mass loss rate	log(g s ⁻¹)	U(10.3, 13)	$12.1_{-1.1}^{+0.5}$	
Log XUV Luminosity	log(erg s ⁻¹)	U(26, 29)	> 27	In the model, all photons were assumed to have energies of 20 eV. See Methods: Outflow model for implications.
Log stellar wind velocity	log(km s ⁻¹)	U(1.5, 3)	-	The posterior effectively returns the prior (i.e., the parameter is unconstrained by the data).
				Planet b
Mass	M _⊗	N(4.0, 0.9)	$3.97^{+0.92}_{-0.83}$	Prior based on the mass and uncertainty estimated by ref. 17
Log hydrogen mass loss rate	log(g s ⁻¹)	see note	$9.29_{-1.01}^{+0.37}$	The prior imposes an upper bound on mass loss efficiency. See Methods: Outflow model for more details.
Log isothermal sound speed	log(km s ⁻¹)	U(0, 1.35)	1. $12^{+0.11}_{-0.58}$	An additional prior disallows sound speeds requiring the temperature of a fully-ionised outflow to be $\!>\!30,\!000$ K.
Outflow angle	radians	U(π/2, π)	-	The posterior effectively returns the prior (i.e., the parameter is unconstrained by the data).
				Planet c
Mass	M _☉	N(5.3, 1.8)	$5.2^{+1.5}_{-1.5}$	Prior based on the mass and uncertainty estimated by ref. 17
Log hydrogen mass loss rate	log(g s ⁻¹)	see note	$9.50_{-0.48}^{+0.39}$	The prior imposes an upper bound on mass loss efficiency. See Methods: Outflow model for more details.
Log isothermal sound speed	log(km s ⁻¹)	U(0, 1.35)	$0.61_{-0.28}^{+0.24}$	An additional prior disallows sound speeds requiring the temperature of a fully-ionised outflow to be $> 30,000 \; \text{K}$.
Outflow angle	radians	U(π/2, π)	> 1.72	The fit favours values near π .
			Pı	re-transit Lyman-α Flux Scaling Factor
2021 June	-	-	1.08 ± 0.05	-37–69 km s ⁻¹ band.
2022 June	_	-	1.19 ± 0.05	-37–69 km s ⁻¹ band.
2022 Dec	_	_	0.97 ± 0.02	Integrated line.

Uncertainties specify the 16^{th} – 84^{th} confidence interval. U stands for uniform distribution and N for normal distribution. Where the posterior is given as a lower limit, the lower limit is taken as the 5^{th} percentile.